ROYAL SOCIETY
OF CHEMISTRY

PAPER

Check for updates

Anchoring and space-confinement effects to form ultrafine Ru nanoclusters for efficient hydrogen generation†

Jian Yang, [ID] [a] Heng Guo,[a] Shulin Chen,[c] Yulan Li,[a] Chao Cai,[b] Peng Gao,[c] Liping Wang, [ID] [a] Yanning Zhang, [ID] [b] Rujie Sun,[d] Xiaobin Niu [ID] *[a] and Zhiming Wang[b]

Developing highly efficient, durable, and low-cost catalysts for the hydrogen evolution reaction (HER) is an eternal pursuit for scientists to replace Pt-based catalysts. The fundamental ways to boost the performance of electrocatalysts are improving the intrinsic activity of each active site and increasing the number of exposed active sites. Herein, we report a novel approach to synthesize ultrafine Ru nanocluster catalysts embedded in a nitrogen-doped carbon framework. To illustrate this strategy, Ru atoms are immobilized in tetra-aminephthalocyanine ($RuPc-NH_2$) by $Ru–N_4$ bonds and subsequently confined by graphene oxide (GO) nanosheets in space. After pyrolysis treatment, ultrafine Ru nanoclusters (average size 1.03 ± 0.23 nm) stabilized by an N-doped carbon framework with a 23.7 wt% Ru content (Ru@NG) are prepared. Importantly, Ru@NG shows excellent HER performance with small overpotentials (20.3 mV in 1.0 M KOH and 42.7 mV in 0.5 M H_2SO_4) at 10 mA cm^{-2}, a high active site number (3.54×10^{-3} mol g^{-1}) and robust durability both in alkaline and acidic environments. Therefore, this work provides a promising substitute for expensive Pt-based catalysts.

1 Introduction

Hydrogen, as the most promising sustainable energy carrier, has been recognized as an ideal alternative to traditional fossil fuels for its high gravimetric energy density, carbon neutrality and earth-abundance.[1–4] Among the various routes of hydrogen production, electrochemical water splitting is considered as a highly attractive approach to gain hydrogen owing to its low-energy consumption, high-purity and environment friendly process.[5] In the water electrolysis process, efficient active electrocatalysts are imperative to reduce the overpotential of the hydrogen evolution reaction and enhance the hydrogen production rate. Up to now, platinum (Pt) and Pt-based materials, as the 'Holy Grail' of HER electrocatalysts, have remained the best HER catalysts with negligible overpotential and excellent long-term stability.[6,7] However, the widespread commercialization of Pt-based electrocatalysts is limited due to their low natural abundance and high cost. In addition, the catalytic activity of Pt has an obvious decrease in alkaline solutions, owing to the poor proton source of alkaline electrolytes.[8]

In order to replace Pt-based catalysts, extensive efforts have been undertaken to design cost-effective electrocatalysts for the HER based on earth-abundant elements.[9,10] In principle, catalyst design strategies are aiming to increase the number of exposed active sites on a given electrode as well as improve the intrinsic activity of each active site.[11] For the first strategy, downsizing metal clusters is a consensual effective way to increase the number of exposed active sites. For example, single atom catalysts represent the lowest size limit to expose the most active sites in catalysts with maximum atom utilization.[12,13] However, pursuing ultrafine size metal nanoclusters as well as high content loading in carbon framework is a great challenge owing to the migration and agglomeration of metal atoms during preparation and catalytic processes, especially for single atom catalysts.[14] For the second strategy, optimizing the electronic structures of catalysts with close to zero hydrogen adsorption free energy ($\Delta G_H \approx 0$) is a fundamental way to improve the intrinsic activity of each active site, which can provide a fast proton/electron-transfer and a quick hydrogen release process.[15] For example, heteroatom doping (C, N, P, or S), alloying (Co, Ni, Fe, Mo, and W) and formation of core–shell structures in metal catalysts have been demonstrated as effective methods to obtain highly efficient activity.[16–27] However, their high overpotential compared to that of Pt-based catalysts increases energy consumption and hence reduces economic competitiveness.

[a]*School of Materials and Energy, State Key Laboratory of Electronic Thin Film and Integrated Devices, University of Electronic Science and Technology of China, Chengdu 610054, China. E-mail: xbniu@uestc.edu.cn*

[b]*Institute of Fundamental and Frontier Sciences, University of Electronic Science and Technology of China, Chengdu 610054, P. R. China*

[c]*Collaborative Innovation Center of Quantum Matter, Beijing 100871, China*

[d]*Wavetronix LLC, Provo, UT 84606, USA*

This journal is © The Royal Society of Chemistry 2018

J. Mater. Chem. A, 2018, **6**, 13859–13866 | 13859

In addition, most of the above-mentioned catalysts do not bear the extreme environment in acidic and alkaline electrolytes for long-term operation. Therefore, improving the long-term stability of catalysts is still a major challenge. Recently, other cheaper Pt-group metals have been investigated for the HER owing to their similar chemical inertness.[28] For example, the price of ruthenium (Ru) is $42 per oz, only 4% of the Pt price, which is very competitive for commercialization.[29] Mahmood reported a Ru@C_2N catalyst with Pt-like activity in both acidic and alkaline environments.[30] Pu studied RuP$_2$-based catalysts for efficient hydrogen production at all pH values.[31] Su also published Ru–Co nanoalloys as electrocatalysts for generating hydrogen in alkaline media.[32] Chen and Ye investigated graphene and graphene-like based Ru catalysts for the HER.[33,34] All these mentioned research studies share similarities: (i) nitrogen dopants play a crucial role in improving electrocatalytic activity for the HER and (ii) Ru salts as the metal source are dispersed into an organic precursor (*e.g.*, melamine, phytic acid, or metal–organic support) or graphene-based framework and subsequently pyrolysed to form carbon-based Ru catalysts with nitrogen dopants. However, the sites of Ru and N dopants are randomly distributed during the pyrolysis process. Meanwhile, the migration and agglomeration of Ru metal species are inevitable, which lead to a low active site density and limit electrocatalytic performance.[35]

In this work, we present a carefully designed method for preparing ultrafine Ru nanoclusters embedded in N-doped carbon-based catalysts formed by the synergic effect of anchoring and space-confinement toward the efficient HER. Our strategy includes three steps: (1) synthesizing Ru tetraamine-phthalocyanine (RuPc-NH$_2$) to anchor Ru atoms in the center of the phthalocyanine macrocycle by Ru–N$_4$ bonding; (2) two-dimensional materials (*e.g.*, graphene oxide (GO) and graphitic carbon nitride (g-CN)) are introduced to confine RuPc-NH$_2$ in space; (3) pyrolyzing the precursors and forming an N-doped carbon-based framework to stabilize Ru nanoclusters. Then, ultrafine Ru nanocluster catalysts (average diameter size 1.0–2.0 nm) with a high Ru content (up to 23.6 wt%) are prepared. The series of Ru-based catalysts exhibit outstanding activity and robust durability in all pH spectrums, particularly superior to Pt/C in alkaline solutions. Furthermore, the number of active sites for the Ru-based catalyst was confirmed by underpotential deposition of copper (Cu-UPD) which shows that anchoring and space-confinement synergic effects can improve the number of exposed active sites effectively.

2 Results and discussion

2.1 Fabrication and structural characterization

The preparation procedure of ultrafine Ru nanoclusters embedded in nitrogen doped carbon catalysts is summarized in Scheme 1. In the RuPc-NH$_2$ metal–organic complex, a Ru atom is precisely anchored at the center of the N$_4$-macrocycle by the Ru–N$_4$ chemical bond, which will diminish the migration and agglomeration of Ru atoms during the pyrolyzing process (as seen in Fig. S1–S3†). Therefore, carbon-based catalysts with Ru and N co-dopants are prepared *via* directly pyrolyzing the RuPc-
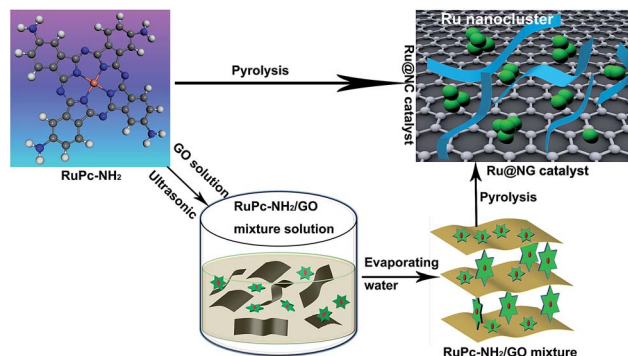
Scheme 1 Schematic illustration of the synthetic route of ultrafine Ru nanoclusters embedded in a N-doped carbon catalyst. One route is directly pyrolyzing the RuPc-NH$_2$ precursor (chemical anchor effect); another route is pyrolyzing the RuPc-NH$_2$/GO mixture (anchoring and space-confinement synergic effects).

NH$_2$ precursor, which is termed Ru@NC. Owing to the high content of Ru (15 wt%) in the RuPc-NH$_2$ precursor, the aggregation and formation of large-sized nanoparticles are unavoidable, and then GO or g-CN nanosheets (Fig. S4†) are introduced to confine RuPc-NH$_2$ in space by the ultrasonic intercalation method.[36] In the RuPc-NH$_2$/GO mixture, RuPc-NH$_2$ is confined and immobilized by the GO nanosheets owing to the hydrogen bond interaction or electrostatic incorporation between tetraamino substituents and the carboxy group (as seen in Fig. S5 and S6†). During a thermal decomposition–reduction process, the migration and agglomeration of Ru atoms are effectively prevented through the combined effect of chemical-anchoring from the Ru–N$_4$ chemical bond and space-confinement from the GO nanosheets. Meanwhile, the GO is reduced to N-doped graphene at high temperature. Finally, the target catalyst Ru@NG is successfully synthesized. The catalyst of Ru@N-g-CN prepared by introducing g-CN nanosheets is also obtained *via* a similar procedure to that of Ru@NG. For comparison, Ru/NC is also prepared through directly pyrolyzing 4-nitrophthalonitrile and the RuCl$_3$ mixture. The Ru nanoparticles (Ru-np) are also selected as a control sample to illuminate our strategy in this work.

The resultant catalysts Ru@NC and Ru@NG are dark black fine powders, but the control sample Ru/NC is granular (Fig. S7†). The morphologies of various samples (including Ru@NG, Ru@NC, Ru@N-g-CN, Ru/NC, and Ru-np) were examined by scanning electron microscopy (SEM) (Fig. S8 and S9†), and no distinct differences between Ru@NG, Ru@NC, and Ru@N-g-CN were observed at the micrometer scale, which exhibit typical porous structures of carbon-based materials. However, the structure of Ru/NC is compact (Fig. S9c†), which will be unfavorable for exposure active sites. The Ru-np as a control sample in Fig. S9d† are uniform nanospheres with a diameter size of ~30 nm. In order to get further insight into the morphologies of Ru-based catalysts, aberration corrected transmission electron microscopy (TEM) and energy-dispersive X-ray spectroscopy (EDX) were conducted. As shown in Fig. 1a, S10a and b,† and Fig. 1b, the ultrafine Ru nanoclusters of Ru@NG are uniformly distributed in the layered graphite
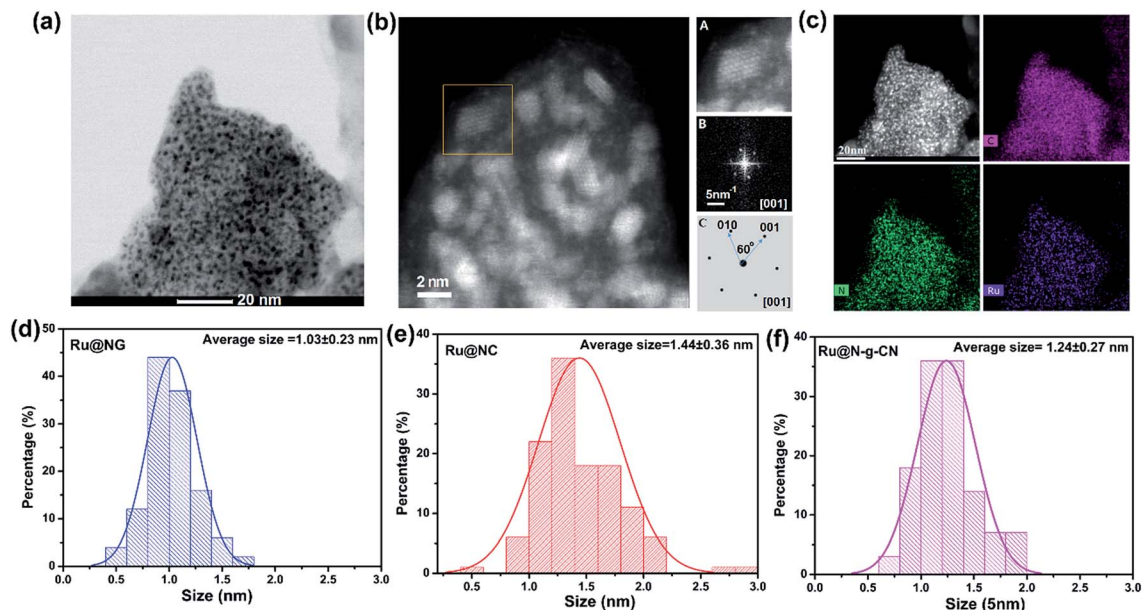
Fig. 1 (a) Bright field (BF)-STEM image of the Ru@NG catalyst. (b) HAADF-STEM image of Ru@NG (inset: (A) magnified image of a Ru nanocluster, (B) the corresponding FFT pattern and (C) simulated electron diffraction pattern). (c) HAADF-STEM image and the corresponding elemental mapping distributions. (d–f) Size distribution of Ru nanoclusters in Ru@NG, Ru@NC and Ru@N-g-CN.

matrix, suggesting that the aggregation of large-sized Ru nanoparticles is hampered. The magnified high angle annular dark field (HAADF) scanning transmission electron microscopy (STEM) image (inset of Fig. 1b) clearly shows the crystalline nature of Ru nanoclusters, and the corresponding fast-Fourier transform (FFT) pattern is identified to be the [001] zone axis with a d-spacing of 0.233 and 0.238 nm for the crystal lattices. Then, the EDX-mappings in Fig. 1c further verify the highly homogeneous distribution of C, N, and Ru in Ru@NG, and the Ru content is about 25.28 wt% (Fig. S11†). In addition, the Ru contents in Ru@NC, Ru@NG, Ru@N-g-CN and Ru/NC were calculated by thermogravimetric analysis (TGA) in an air atmosphere, and the results are about 26.5 wt%, 23.7 wt%, 28.5 wt% and 30.5 wt%, respectively (as seen in Fig. S12†). The size distribution of the Ru nanoclusters in Ru@NC, Ru@NG and Ru@N-g-CN are further investigated based on the TEM images in Fig. S10b, d and f.† As shown in Fig. 1d–f, the average sizes of the Ru@NC, Ru@NG, and Ru@N-g-CN are 1.44 ± 0.36 nm, 1.03 ± 0.23 nm and 1.24 ± 0.27 nm, respectively. This shows that the average sizes of Ru nanoclusters are relatively smaller after introducing GO and g-CN. We can infer that the migration and aggregation of Ru atoms are effectively diminished by space-confinement of GO or g-CN nanosheets in the pyrolyzing process. Therefore, the homogeneously distributed ultrafine Ru nanoclusters with optimized size distribution will facilitate more exposed active sites, thus improving the electrocatalytic activity.

X-ray diffraction (XRD) was employed to identify Ru@NC, Ru@NG, Ru@N-g-CN, and Ru/NC. In Fig. 2a, only Ru/NC shows obvious diffraction peaks, which can be ascribed to hexagonal Ru (JCPDS no. 06-0663), and the broad peak at 25° is ascribed to the (002) plane of N-doped graphite. The other catalysts show no diffraction peak of Ru crystal, indicating the weak crystallinity

of Ru in the Ru@NC, Ru@NG, and Ru@N-g-CN, which is in accordance with the TEM images. Fig. 2b presents the Raman spectrum of various samples. All the samples exhibit the D (~1348 cm^{-1}) and G (~1586 cm^{-1}) bands and a weak 2D (~2800 cm^{-1}) band, which are the characteristic features of graphitic carbon with a low degree of graphitization. The intensity ratio (I_D/I_G) can reflect the defect degree of carbon. In Fig. 2b (inset), the I_D/I_G of Ru@NG is larger than those of others, indicating a plenty of defects in the carbon framework. This phenomenon is attributed to the N dopants and concomitant absence of C atoms in part derived from the intrinsic defect of GO. These defects can alter charge and spin distribution and then affect the catalytic activities. The detailed surface area and pore size distribution are further investigated with the N$_2$ adsorption–desorption isotherms (Fig. 2c and S13†) for Ru@NG, Ru@NC, and Ru@N-g-CN. As seen in Fig. 2c, Ru@NG exhibits a specific surface area of 73.9 m^2 g^{-1}, a pore volume of 0.170 cm^3 g^{-1} with pore size distribution mainly in the range of 2–20 nm, suggesting its mesoporous characteristics without rigid aggregates. The results of Ru@NC (surface area of 55.7 m^2 g^{-1} and pore volume of 0.183 cm^3 g^{-1}) and Ru@N-g-CN (surface area of 58.4 m^2 g^{-1} and pore volume of 0.165 cm^3 g^{-1}) are shown in Fig. S13† with similar absorption/desorption curves. All data from the three samples are very close except the surface area of Ru@NG, probably due to the high surface area of graphene. Meanwhile, the element species and chemical states of Ru@NG were also confirmed by X-ray photoelectron spectroscopy (XPS). As shown in Fig. 2d, the Ru@NG possesses C, N, Ru, and O elements, agreeing well with the TEM and EDX mapping results. The high-resolution C 1s and Ru 3d spectra of Ru@NG (Fig. 2d, inset) can be deconvoluted into four individual peaks, attributed to C=C (284.2 eV), C–N (285.7 eV), Ru 3d5/2 (280.1 eV) and Ru 3d3/2 (284.4 eV), respectively. The high-
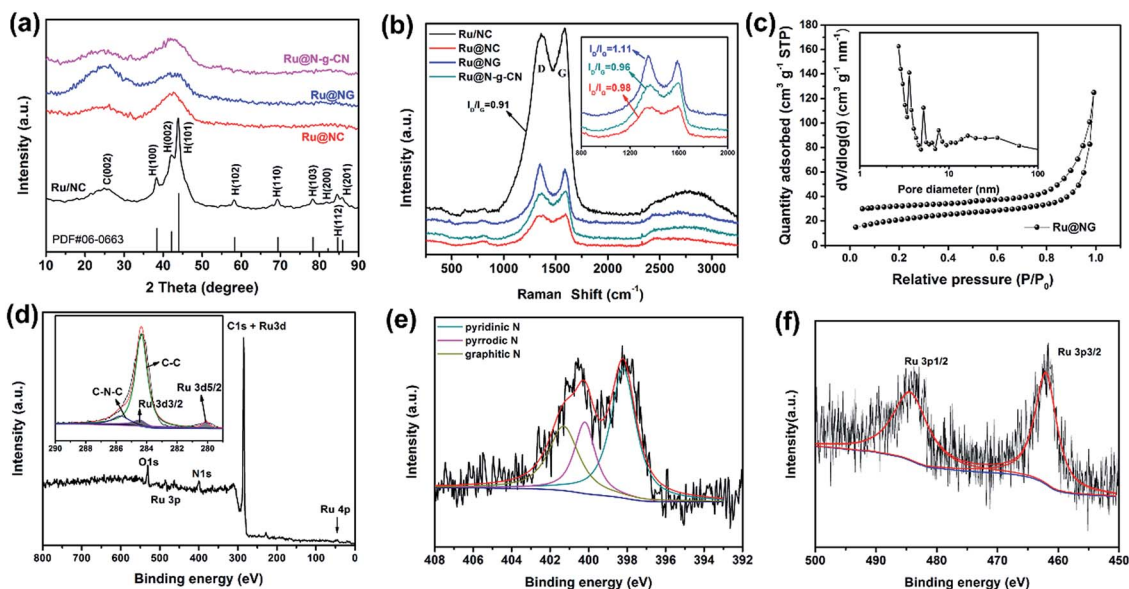
Fig. 2 (a and b) XRD patterns and Raman spectra of the Ru-based catalysts. (c) N_2 adsorption/desorption isotherms of Ru@NG, the inset is the corresponding pore size distribution. (d) XPS survey full scan (inset: high resolution C 1s + Ru 3d). (e) High-resolution N 1s and (f) Ru 3p spectra of Ru@NG.

resolution N 1s spectrum shown in Fig. 2e is deconvoluted into three peaks at 398.4, 400.2 and 401.3 eV, attributed to pyridinic N (48.8%), pyrrolic N (22.2%) and graphitic N (29.0%), respectively. The Ru^0 is further confirmed by the high-resolution Ru 3p spectrum with peaks at 461.6 and 484.0 eV, attributed to Ru 3p3/2 and Ru 3p1/2 of Ru^0. The high-resolution O 1s spectrum (shown in Fig. S14†) is also deconvoluted into three peaks at 530.0 eV (Ru/RuOx), 530.9 eV (O–H), and 532.3 eV (C=O), indicating traces of Ru oxide on the surface of Ru nanoclusters. The other XPS spectra of Ru@NC, Ru@N-g-CN and Ru/NC are illustrated in Fig. S15–S18,† and all curves are similar to that of Ru@NG, suggesting the similar chemical components.

2.2 HER electrocatalytic performance

The HER performances of the various catalysts were evaluated in Ar saturated 1.0 M KOH, 0.5 M H_2SO_4 and 1.0 M PB aqueous solutions, separately. All the results were obtained in a conventional three-electrode cell using a saturated Ag/AgCl electrode as the reference electrode and a graphite rod as the counter electrode. Fig. 3a and b show the linear sweep voltammetry (LSV) curves of the Ru-based catalysts in alkaline and acidic media. Ru@NC, Ru@N-g-CN, and Ru@NG present electrocatalytic activities even superior to that of Pt/C in 1.0 M KOH alkaline solution. Importantly, Ru@N-g-CN and Ru@NG only need ~20 mV at 10 mA cm^{-2} HER current density, which is 13 mV lower than that of commercial 20 wt% Pt/C (~33 mV) and 5 mV lower than that of Ru@NC (~25 mV). One reason is probably due to the faster water dissociation rate in Ru-based catalysts than in the Pt-based surface ($H_2O + e^- + M \leftrightharpoons M - H_{ad} + OH^-$, H_{ad}, historically termed "overpotential hydrogen").[8,37] These extraordinary performances are among the smallest overpotential values for transition-metal based catalysts,[31] and thus

this indicates that introducing GO and g-CN 2D materials as a space-confinement framework will enhance the catalytic performances of Ru-based catalysts for the HER. This observation is also confirmed in acidic and neutral electrolytes. As can be seen in Fig. 3b, Pt/C exhibits outstanding HER activity with a near-zero onset overpotential in an acidic environment. Ru@NC also shows a higher catalytic activity, only needing an overpotential of ~55 mV to achieve 10 mA cm^{-2}. Significantly, the overpotentials of Ru@N-g-CN and Ru@NG are further decreased to ~43 mV at 10 mA cm^{-2}. Moreover, the HER performances of the series of Ru-based catalysts in 1.0 M phosphate buffered solution (PB, pH = 7.05) are shown in Fig. S19.† Pt/C is still an excellent catalyst for the HER in a neutral environment with an overpotential of 53 mV at 10 mA cm^{-2}. Owing to the inherently slow kinetics in neutral solution,[38] the electrocatalytic activities of the Ru-based catalysts are decreased compared to their performances in acidic and alkaline solutions. In spite of this, the Ru-based catalysts still show considerable HER performances in neutral solution with overpotentials of 165, 144, and 128 mV (at 10 mA cm^{-2}) for Ru@NC, Ru@N-g-CN and Ru@NG, respectively.

The Tafel slopes of the Ru-based catalysts are shown in Fig. 3c and d corresponding to various electrolytes. In alkaline medium (Fig. 3c), the Tafel slopes of Ru@NC, Ru@N-g-CN and Ru@NG are 29, 29 and 26 mV dec^{-1}, respectively, which are less than that of Pt/C (40 mV dec^{-1}) and match with the LSV curves shown in Fig. 3a. This result indicates that the Volmer–Tafel mechanism is the rate-limiting step in alkaline medium. However, in acidic medium, the Tafel slopes of Ru@NC, Ru@N-g-CN and Ru@NG are determined to be 56, 55 and 55 mV dec^{-1} (as seen in Fig. 3d), respectively, suggesting that the Volmer–Heyrovsky reaction is the rate-determining step. With no surprise, the Tafel slopes of these Ru-based catalysts are

13862 | J. Mater. Chem. A, 2018, 6, 13859–13866

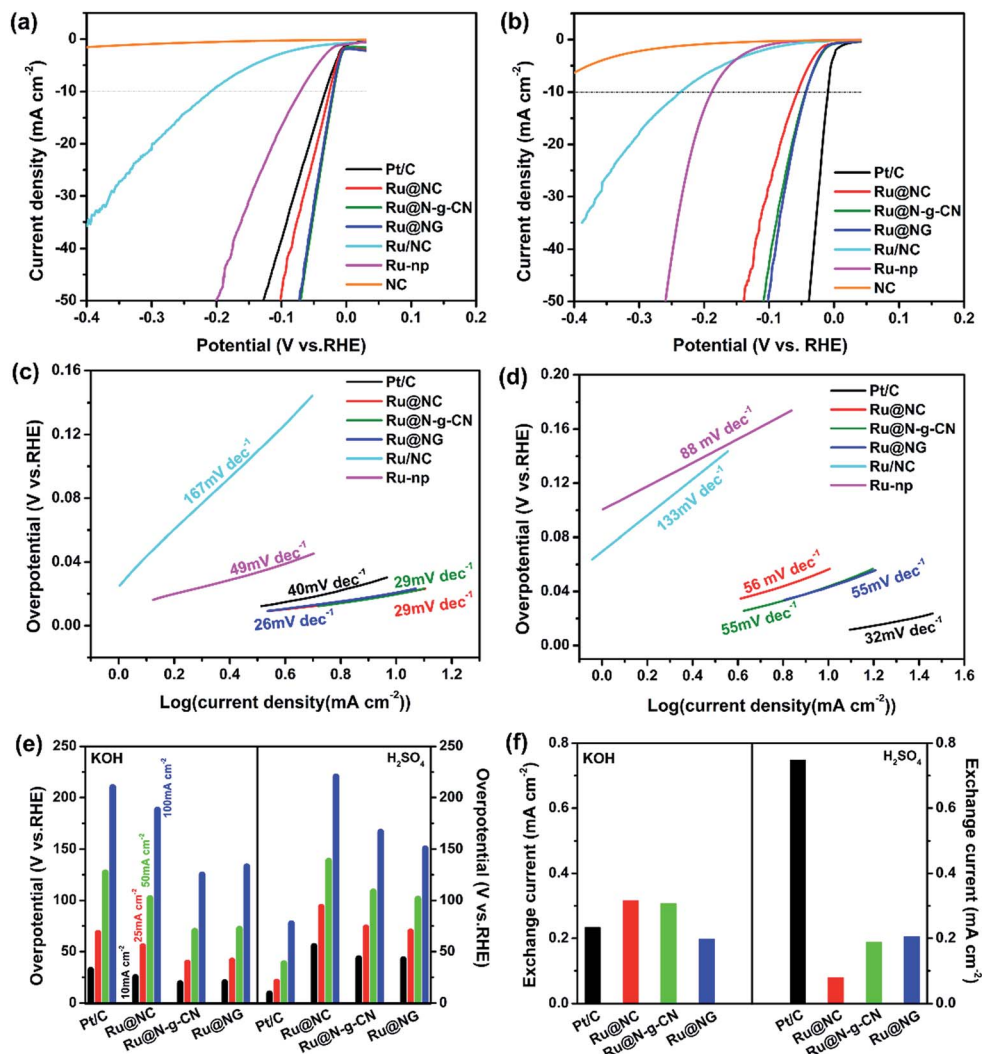This journal is © The Royal Society of Chemistry 2018

Fig. 3 Electrocatalytic HER performance measurements of the catalysts in alkaline and acidic solutions: Polarization curves of various catalysts (Ru@NC, Ru@N-g-CN, Ru@NG, Ru/NC, Ru-np, NC and 20 wt% Pt/C) with a scan rate of 2 mV s^{-1} in (a) 1.0 M KOH and (b) 0.5 M H$_2$SO$_4$; (c and d) the corresponding Tafel plots obtained from the polarization curves. (e) Overpotentials at various current densities (10, 25, 50, and 100 mA cm^{-2}) of Ru@NC, Ru@NG, Ru@N-g-CN and Pt/C in alkaline (left) and acidic (right) solutions. (f) Exchange current densities of Ru@NC, Ru@NG, Ru@N-g-CN and Pt/C in alkaline (left) and acidic (right) solutions.

enhanced by about 2–3-fold in the neutral medium, suggesting the inherently slow kinetics of the HER under this condition (Fig. S19b†). For comparison, the Ru/NC, Ru-np, and NC (metal-free N-doped carbon catalyst prepared by pyrolyzing zinc phthalocyanine (ZnPc) and evaporating Zn simultaneously[39]) catalysts were also tested with the same processes. The poor performances, attributed to the limited active site density and lower intrinsic activity,[30,32] of these reference catalysts further approve that the synergic effect of chemical anchoring and physical blockage can significantly enhance the efficiency in HER electrocatalysis. In order to gain further insight into the excellent catalytic activities of Ru@NC, Ru@N-g-CN and Ru@NG catalysts, the overpotentials at high current density (e.g. at 25, 50, 100 mA cm^{-2}) are displayed in Fig. 3e. We can conclude that Ru@N-g-CN and Ru@NG are among the best catalysts loaded on a glassy carbon electrode in recent reports towards the HER in alkaline medium at a wide range of current

densities (Table S1†). The exchange current densities of the Ru-based catalysts obtained by extrapolating the Tafel plots to the Y-axis are shown in Fig. 3f. These results correspond to the LSV curves and Tafel plots, indicating the superior intrinsic electrocatalytic activity of the Ru-based catalysts.

Long-term durability is another important requirement for HER catalysts, especially in extreme environments. Therefore, we evaluated the long-term durability of Ru@NC, Ru@N-g-CN and Ru@NG at a constant overpotential. Meanwhile, commercial Pt/C was used as the benchmark. As shown in Fig. 4a and S20,† Pt/C shows obvious degradation in the time-dependent current density (i–t) test (the inset of Fig. 4a). Compared to the initial polarization curve of Pt/C, the LSV curve obtained in alkaline medium presents a negative shift (about 35 mV at 10 mA cm^{-2}), indicating the poor durability of Pt/C in an alkaline environment. Interestingly, the Ru@NC shows good durability both in acidic and alkaline media as shown in Fig. 4b. 80% of
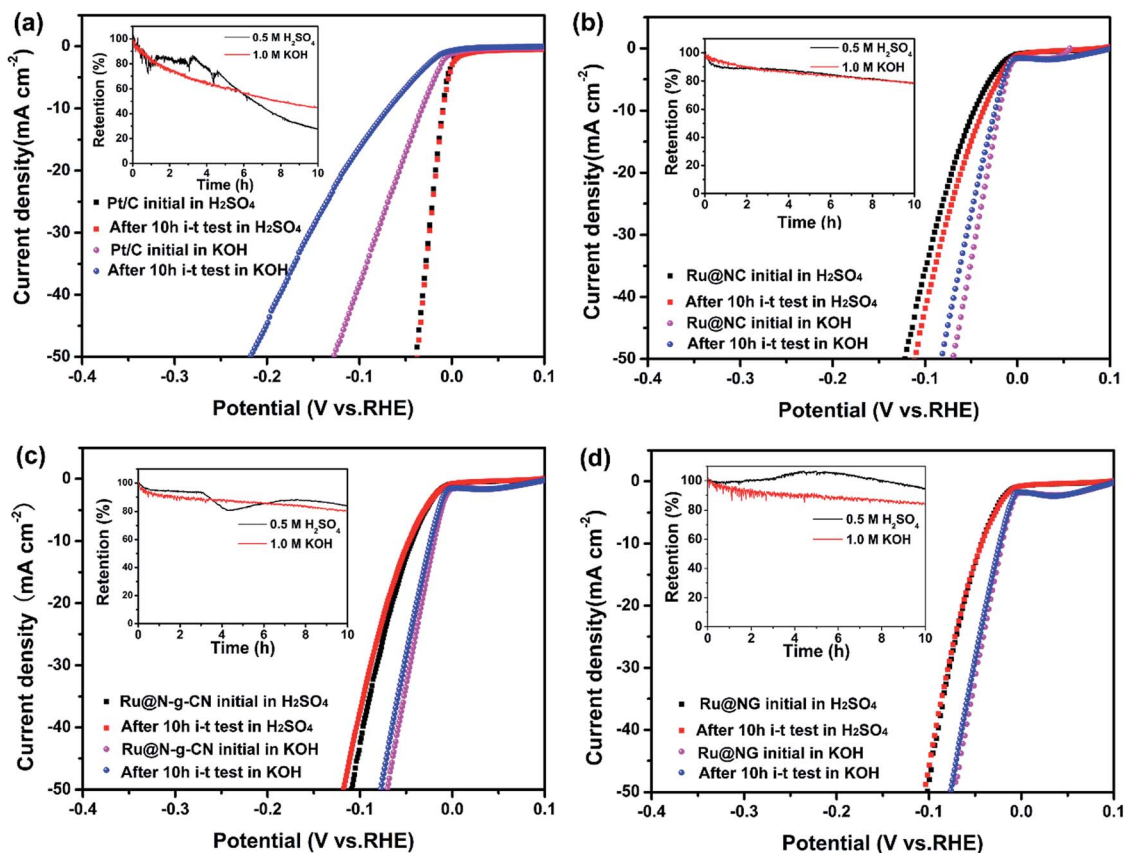
Fig. 4 Long-term durability of Pt/C (a), Ru@NC (b), Ru@N-g-CN (c) and Ru@NG (d) in acidic and alkaline solutions. All the polarization curves were recorded before and after a 10 h i–t test at a constant potential. The insets show the retention of time-dependent current density curves in acidic and alkaline solutions, corresponding to the Pt/C, Ru@NC, Ru@N-g-CN and Ru@NG catalysts.

the current density of Ru@NC is still maintained in the i–t test after 10 h loading in acidic medium. Meanwhile the polarization curve of Ru@NC shows an ~10 mV (10 mA cm^{-2}) positive potential shift instead of a negative shift. Under the alkaline conditions, the polarization curve of Ru@NC shifts negatively only by ~4 mV at 10 mA cm^{-2}. Furthermore, the long-term durability of Ru@N-g-CN and Ru@NG is further enhanced *via* introducing g-CN or GO in the precursors (Fig. 4c and d), in which the retention of current density is still more than 85%, and the LSV curves are almost overlapping the initial ones both in the acidic and alkaline media. The durability of the Ru-based catalysts in neutral medium is also studied, and the results are shown in Fig. S21,† which displays acceptable long-term stabilities. The high durability of Ru@N-g-CN and Ru@NG is possible due to the further encapsulation of N-doped carbon materials, which can effectively prevent the Ru nanocluster corrosion.

2.3 Mechanism analysis derived from the number of exposed active sites

The fundamental understanding of the high electrocatalytic activities of Ru and N co-doped carbonaceous catalysts have been reported by Mahmood.[30] Ru species embedded into an N doped carbon framework would optimize the metal–hydrogen (M–H) bonding value, resulting in highly efficient HER activities. This mechanism improves the intrinsic activity of each

active site and falls into one of the two strategies we proposed. On the other hand, another strategy is to increase the number of exposed active sites on a given electrode through artificial designs. As shown in Fig. 5a, the aggregation of Ru species is accelerated during the thermal reducing and the pyrolyzing processes when directly carbonizing RuCl$_3$ and the organic precursor mixture, resulting in a random size distribution and dispersion of large-sized Ru nanoparticles in the carbon-based framework.[40] In our research the Ru species are immobilized by the chemical-anchoring and space-confinement synergic effect, and therefore ultrafine Ru nanoclusters are confined to a rational size range with uniform size distribution during the pyrolyzing process, thus significantly increasing the number of exposed active sites. In order to prove our proposal, the number of active sites (n), electrochemically active surface area (ECSA) and turnover frequency (TOF) were estimated by the under-potential deposition of copper (Cu-UPD) method. As shown in Fig. 5b and S22 and 23,† the n of Ru@NC, Ru@NG and Ru@N-g-CN are 1.55×10^{-3}, 3.54×10^{-3} and 2.85×10^{-3} mol g^{-1}, and the corresponding ECSA are 92.5, 162.6, and 130.7 m^2 g^{-1}, respectively. As a comparison, Ru/NC shows lower n (1.10×10^{-3} mol g^{-1}) and ESCA (50.4 m^2 g^{-1}). This result suggests that the increased number of exposed active sites on a given electrode is ascribed to the introduction of GO and g-CN nanosheets. Meanwhile, the introduction of nanosheets also
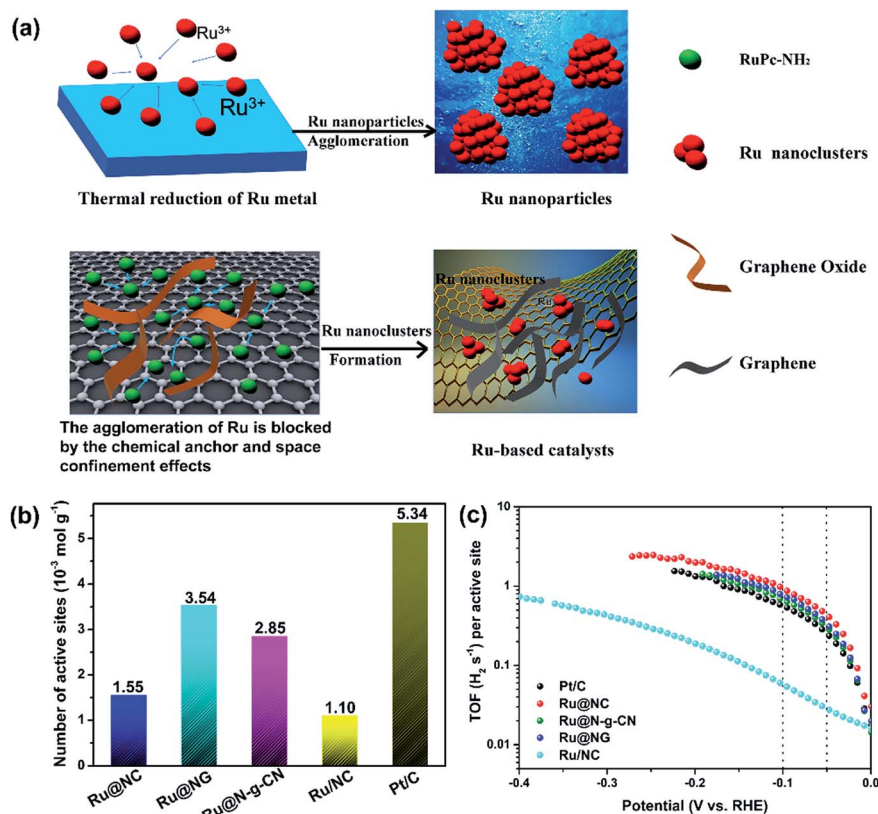
Fig. 5 (a) The schematic illustrating the combined effect of chemical anchoring and physical blockage to obtain confined Ru nanoclusters embedded in N-doped carbon-based catalysts. (b) The number of exposed active sites in the Ru based catalysts calculated from Cu-UPD. (c) TOF values of the Ru based catalysts and Pt/C in 1.0 M KOH solution.

leads to the firm encapsulation of Ru nanoclusters, resulting in the remarkably robust stability of the Ru-based catalysts. The TOF values for each active site of Ru@NC, Ru@NG, Ru@N-g-CN, Ru/NC, and Pt/C in alkaline and acidic electrolytes are calculated based on the corresponding n and LSV curves. As shown in Fig. 5c, S24, and Table S2,† the TOF values of Ru@NC, Ru@NG, and Ru@N-g-CN are significantly enhanced compared with that of Ru/NC and even larger than that of Pt/C in alkaline solution. The TOF values of Ru@NG and Ru@N-g-CN are slightly smaller than that of Ru@NC, probably due to the coating layers of N-doped graphite. The electrochemical double layer capacitance (C_{dl}) of the Ru-based catalysts were measured using the CV method to evaluate the effective surface areas of the solid–liquid interface (Fig. S25 and 26).† The catalysts (Ru@NC, Ru@NG and Ru@N-g-CN) exhibit a much higher C_{dl} than Ru/NC, proving the plentiful exposed active sites and excellent HER performance.

3   Conclusions

In summary, a new method for synthesizing Ru-based catalysts (Ru@NC, Ru@NG and Ru@N-g-CN) with a high number of exposed active sites and superior intrinsic activities for the HER is demonstrated. Due to the chemical-anchoring and space-confinement effects, up to 23–28 wt% Ru content nanoclusters with 1–2 nm diameter in size are uniformly embedded

into the N-doped carbon framework. The outstanding catalyst Ru@NG exhibits efficient HER activity and robust long-term durability in all pH spectra. Particularly, Ru@NG shows better HER performance than the commercial 20 wt% Pt/C catalyst in alkaline electrolyte. Another significant result is that the migration and agglomeration of Ru atoms can be effectively prevented by the chemical anchoring of Ru–N$_4$ and space-confinement of GO (or g-CN), which leads to the increasing number of exposed active sites. Meanwhile, introducing GO and g-CN also improves the long-term stability by further encapsulating the Ru nanoclusters. This work provides a novel pathway to rationally design highly efficient HER catalysts by increasing the number of exposed active sites and intrinsic catalytic activity. We believe that this strategy is also beneficial to develop other nitrogen doped carbon-based catalysts with a high content of transition metals.

Conflicts of interest

There are no conflicts to declare.

Acknowledgements

References

1 M. S. Dresselhaus and I. L. Thomas, *Nature*, 2001, **414**, 332–337.

2 J. A. Turner, *Science*, 2004, **305**, 972–974.

3 M. Balat and H. Balat, *Energy Sources, Part A*, 2009, **31**, 1280–1293.

4 X. Tong, Y. Zhou, L. Jin, K. Basu, R. Adhikari, G. S. Selopal, X. Tong, H. Zhao, S. Sun, A. Vomiero, Z. M. Wang and F. Rosei, *Nano Energy*, 2017, **31**, 441–449.

5 P. C. Vesborg, B. Seger and I. Chorkendorff, *J. Phys. Chem. Lett.*, 2015, **6**, 951–957.

6 L. Zhang, Q. Chang, H. Chen and M. Shao, *Nano Energy*, 2016, **29**, 198–219.

7 V. R. Stamenkovic, B. S. Mun, M. Arenz, K. J. Mayrhofer, C. A. Lucas, G. Wang, P. N. Ross and N. M. Markovic, *Nat. Mater.*, 2007, **6**, 241–247.

8 D. Strmcnik, P. P. Lopes, B. Genorio, V. R. Stamenkovic and N. M. Markovic, *Nano Energy*, 2016, **29**, 29–36.

9 X. Zou and Y. Zhang, *Chem. Soc. Rev.*, 2015, **44**, 5148–5180.

10 J. Wang, F. Xu, H. Jin, Y. Chen and Y. Wang, *Adv. Mater.*, 2017, **29**, 1605838.

11 J. D. Benck, T. R. Hellstern, J. Kibsgaard, P. Chakthranont and T. F. Jaramillo, *ACS Catal.*, 2014, **4**, 3957–3971.

12 C. Zhu, S. Fu, Q. Shi, D. Du and Y. Lin, *Angew. Chem., Int. Ed.*, 2017, **56**, 13944–13960.

13 X. F. Yang, A. Wang, B. Qiao, J. Li, J. Liu and T. Zhang, *Acc. Chem. Res.*, 2013, **46**, 1740–1748.

14 T. E. James, S. L. Hemmingson and C. T. Campbell, *ACS Catal.*, 2015, **5**, 5673–5678.

15 R. Parsons, *Trans. Faraday Soc.*, 1958, **54**, 1053–1063.

16 B. Bayatsarmadi, Y. Zheng, Y. Tang, M. Jaroniec and S. Z. Qiao, *Small*, 2016, **12**, 3703–3711.

17 Y. Xu, W. Tu, B. Zhang, S. Yin, Y. Huang, M. Kraft and R. Xu, *Adv. Mater.*, 2017, **29**, 1605957–1605964.

18 L. Yu, H. Zhou, J. Sun, F. Qin, D. Luo, L. Xie, F. Yu, J. Bao, Y. Li, Y. Yu, S. Chen and Z. Ren, *Nano Energy*, 2017, **41**, 327–336.

19 J. Deng, H. Li, S. Wang, D. Ding, M. Chen, C. Liu, Z. Tian, K. S. Novoselov, C. Ma, D. Deng and X. Bao, *Nat. Commun.*, 2017, **8**, 14430.

20 X. Wang, X. Gan, T. Hu, K. Fujisawa, Y. Lei, Z. Lin, B. Xu, Z. H. Huang, F. Kang, M. Terrones and R. Lv, *Adv. Mater.*, 2017, **29**, 1603617.

21 X. Tong, X.-T. Kong, Y. Zhou, F. Navarro-Pardo, G. S. Selopal, S. Sun, A. O. Govorov, H. Zhao, Z. M. Wang and F. Rosei, *Adv. Energy Mater.*, 2017, **8**, 1701432.

22 J. Yang, C. Cai, Y. Li, L. Gao, H. Guo, B. Wang, B. Pu and X. Niu, *Electrochim. Acta*, 2018, **262**, 48–56.

23 H. Tabassum, W. Guo, W. Meng, A. Mahmood, R. Zhao, Q. Wang and R. Zou, *Adv. Energy Mater.*, 2017, **7**, 1601671–1601677.

24 H. Wang, S. Min, C. Ma, Z. Liu, W. Zhang, Q. Wang, D. Li, Y. Li, S. Turner, Y. Han, H. Zhu, E. Abou-Hamad, M. N. Hedhili, J. Pan, W. Yu, K. W. Huang, L. J. Li, J. Yuan, M. Antonietti and T. Wu, *Nat. Commun.*, 2017, **8**, 13592.

25 Q. Han, Z. H. Cheng, J. Gao, Y. Zhao, Z. P. Zhang, L. M. Dai and L. T. Qu, *Adv. Funct. Mater.*, 2017, **27**, 1606352.

26 J. Zhang, L. Qu, G. Shi, J. Liu, J. Chen and L. Dai, *Angew. Chem., Int. Ed.*, 2016, **55**, 2230–2234.

27 J. X. Feng, H. Xu, S. H. Ye, G. Ouyang, Y. X. Tong and G. R. Li, *Angew. Chem., Int. Ed.*, 2017, **56**, 8120–8124.

28 J. Zhang, G. Wang, Z. Liao, P. Zhang, F. Wang, X. Zhuang, E. Zschech and X. Feng, *Nano Energy*, 2017, **40**, 27–33.

29 X. Kong, K. Xu, C. Zhang, J. Dai, S. Norooz Oliaee, L. Li, X. Zeng, C. Wu and Z. Peng, *ACS Catal.*, 2016, **6**, 1487–1492.

30 J. Mahmood, F. Li, S. M. Jung, M. S. Okyay, I. Ahmad, S. J. Kim, N. Park, H. Y. Jeong and J. B. Baek, *Nat. Nanotechnol.*, 2017, **12**, 441–446.

31 Z. Pu, I. S. Amiinu, Z. Kou, W. Li and S. Mu, *Angew. Chem., Int. Ed.*, 2017, **56**, 11559–11564.

32 J. Su, Y. Yang, G. Xia, J. Chen, P. Jiang and Q. Chen, *Nat. Commun.*, 2017, **8**, 14969.

33 Z. Chen, J. Lu, Y. Ai, Y. Ji, T. Adschiri and L. Wan, *ACS Appl. Mater. Interfaces*, 2016, **8**, 35132–35137.

34 R. Ye, Y. Liu, Z. Peng, T. Wang, A. S. Jalilov, B. I. Yakobson, S. H. Wei and J. M. Tour, *ACS Appl. Mater. Interfaces*, 2017, **9**, 3785–3791.

35 J. Guo, Y. Li, Y. Cheng, L. Dai and Z. Xiang, *ACS Nano*, 2017, **11**, 8379–8386.

36 S. Brüller, H.-W. Liang, U. I. Kramm, J. W. Krumpfer, X. Feng and K. Müllen, *J. Mater. Chem. A*, 2015, **3**, 23799–23808.

37 Y. F. Cheng, S. K. Lu, F. Liao, L. B. Liu, Y. Q. Li and M. W. Shao, *Adv. Funct. Mater.*, 2017, **27**, 1700359.

38 Y.-Y. Ma, C.-X. Wu, X.-J. Feng, H.-Q. Tan, L.-K. Yan, Y. Liu, Z.-H. Kang, E.-B. Wang and Y.-G. Li, *Energy Environ. Sci.*, 2017, **10**, 788–798.

39 P. Yin, T. Yao, Y. Wu, L. Zheng, Y. Lin, W. Liu, H. Ju, J. Zhu, X. Hong, Z. Deng, G. Zhou, S. Wei and Y. Li, *Angew. Chem., Int. Ed.*, 2016, **55**, 10800–10805.

40 J. Jones, H. Xiong, A. T. DeLaRiva, E. J. Peterson, H. Pham, S. R. Challa, G. Qi, S. Oh, M. H. Wiebenga, X. I. Pereira Hernandez, Y. Wang and A. K. Datye, *Science*, 2016, **353**, 150–154.